Heliyon 10 (2024) e27613

Contents lists available at ScienceDirect

Heliyon

journal homepage: www.cell.com/heliyon

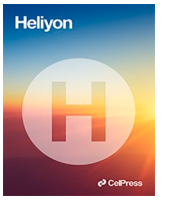

Research article

Vacancy induced enhanced photocatalytic activity of nitrogen doped CuO NPs synthesized by Co-precipitation method

Md Jannatul Ferdous Anik [1], Samiya Rahman Mim [1], Syed Sammo Swapno, Sirajum Munira, Oishy Roy, Md Muktadir Billah [*]

Department of Materials and Metallurgical Engineering, Bangladesh University of Engineering and Technology, Dhaka-1000, Bangladesh

ARTICLE INFO

Keywords:
Co-precipitation
Photoelectron
Photoluminescence
Recombination
Photocatalytic

ABSTRACT

The chemical co-precipitation method, an effective approach in the synthesis of nanomaterials, was used to synthesize CuO nanoparticles (NPs). Structural and morphological modification of undoped and nitrogen (N) doped CuO nanoparticles were studied thoroughly using X-ray diffraction (XRD), FT-IR and field emission scanning electron microscope (FE SEM). Doping effect on defects was investigated using X-ray photoelectron spectroscopy (XPS), Raman spectroscopy and photoluminescence (PL) spectroscopy. Thus, the effect of doping on crystallinity, crystallite size, strain induced in lattice, defects and electron-hole recombination rate were investigated. Optical band gap was calculated using Kubelka-Munk function from the diffuse reflectance spectra (DRS) obtained using ultraviolet visible (UV–Vis) spectroscopy. Finally, photocatalytic performance was studied from rhodamine B (Rh B) degradation and reaction kinetics were analyzed. Maximum degradation efficiency was obtained for 1.0 mol% N doped CuO NPs which also exhibited minimum band gap and lowest electron-hole recombination rate. For the optimum doping concentration, nitrogen was found to create oxygen vacancies while substituting oxygen in the lattice, and thus reduce electron-hole recombination rate and increase photocatalytic degradation rate effectively.

1. Introduction

Wastewater contamination has become a global issue due to its detrimental effect on human life as well as on the animals. On a daily basis, over 2 million tons of waste contaminants are inconsiderably dumped into the open water supplies [1]. Both domestic and industrial effluents such as organic solvents, pesticides, chemical fertilizers, paints, household chemicals, and pharmaceuticals pollute water reserves [2]. The need for wastewater treatment has propelled the advancement of various physico-chemical methods to target specific classes of toxins. The advanced oxidation process (AOP) is often preferred for treating difficult to degrade materials, such as pesticides, organic and synthetic dyes [3,4]. Photocatalysis is a very promising and eco-friendly AOP method since the resulting by-products during treatment are mostly nontoxic [5]. When wastewater containing dyes are exposed to light in presence of the photocatalyst, dye degradation occurs via an oxidation reaction mechanism [6]. The ability of the photocatalyst to produce electron-hole ($e\text{-}h^{+}$) pairs upon light absorption is a key factor in its photocatalytic activity (PCA) [7]. As a strong oxidant, the positive

* Corresponding author.
E-mail address: mbillah@mme.buet.ac.bd (M.M. Billah).
[1] Co-first authors.

https://doi.org/10.1016/j.heliyon.2024.e27613
Received 25 August 2023; Received in revised form 27 February 2024; Accepted 4 March 2024
Available online 13 March 2024

hole can produce hydroxyl free radicals (•OH) while exposed to water or hydroxide ions from the toxic compounds [8]. As these potent oxidants come in contact with toxic organic compounds and pollutants, oxidation reaction take place, which convert the harmful chemicals to CO_2 and H_2O or other less toxic chemicals [9].

Nanostructured semiconductors are used as photocatalysts since materials in nanoscale exhibit unique optoelectronic properties due to quantum confinement effects [10,11]. Metal oxide nanoparticles have been extensively investigated, and many of them, such as TiO_2, CuO, ZnO, MnO_2 and Fe_2O_3, are highly regarded as photocatalysts due to their high surface-to-volume ratio, easy accessibility, exceptional stability across a wide pH range and photo-generated holes [12–15]. However, their photocatalytic activity can be restricted by their partial mineralization, broad band gap and quick recombination of electron-hole pairs [16–18]. Among these oxides, p-type cupric oxide (CuO) with low toxicity, affordability, better physical and chemical stability, a narrow band gap (1.2–2.1 eV) and convenient synthesis processes [8,19], has been extensively explored as a catalyst for various reduction reactions [20]. Hence, it's crucial to assess novel modified CuO catalysts with enhanced photocatalytic activity [21]. Furthermore, CuO has received remarkable attention for applications such as photocatalysis [6], photodetector [22], electrode material for lithium-ion batteries [23], sensors [24], magnetic storage devices, solar cells [25].

Modification and enhancement of structural and optoelectronic properties of CuO nanoparticles (NPs) can be accomplished through synthesis process alteration [26–28], transition metal as well as rare-earth metal doping [21,29], formation of nanocomposites [30] and core-shell nanoparticles [31].Moreover, for any particular synthesis method, such as microwave combustion method [32], hydrothermal method [33], modified sol-gel [14], co-precipitation method [34], structure and properties of the NPs can be further modified by choice of precursors and optimization of various process parameters. Table 1 presents a brief literature review on the photocatalytic performance of pure and modified CuO NPs under various wavelengths of irradiated light and time periods.

The challenges that come with nanocomposite synthesis include intricate preparation techniques and increased energy consumption [38]. Extensive research has been done to find suitable dopants for improved photocatalytic performance of CuO since doping can modify the morphology, band gap and electronic characteristics [33]. However, the performance of transition metal dopants is largely constrained by increased carrier recombination centers and thermal instability [39]. In case of rare earth elements, dopants are quite expensive and meager [1]. Therefore, an effective approach can be selection of non-metallic elements as dopant [7, 37] which are also preferred due to their similarity with oxygen in characteristics. Among these elements, nitrogen (N) can be a better choice due to its low ionization energy and smaller atomic size resulting in formation of a metastable center [40]. Nitrogen mitigates the problem of electron-hole recombination and narrows the band gap by creating N defect states near the valence band. Nitrogen doping was also found to be a beneficial factor as it can potentially create vacancies while replacing oxygen atom from the host lattice, which can effectively enhance photocatalytic performance [9,41–43]. Though a few studies have been reported on synthesis and characterization of CuO NPs doped with different elements, there is still immense scope to enhance their optoelectronic properties especially for photocatalytic application.

In this study, nitrogen doped CuO NPs have been synthesized via co-precipitation method which is considered as a facile technique due to its high efficiency, versatility, low cost, and ability to control particle size and morphology precisely [7]. Compared to other synthesis methods, this approach also offers a number of unique advantages, i.e., an eco-friendly way to produce high-purity nanoparticles with complete control on process parameters, such as pH, temperature and mixing rate [44,45]. Moreover, in co-precipitation method, generation of oxygen vacancies affected by mixing rate have been reported previously as well which is beneficial for photocatalytic activities [46,47]. In order to understand the underlying chemistry, the effect of N doping has been investigated thoroughly on structural, morphological, and optical properties of the NPs. Photocatalytic properties of the pure (0 mol % N doped CuO) and 0.5 mol%, 1.0 mol% and 2.0 mol% N-doped NPs were explored via catalytic degradation of Rh B dye under ultra-violet (UV) light. As it is widely recognized that N doped ZnO and TiO_2 exhibit enhanced photocatalytic properties [48,49], investigation on N doped CuO NPs synthesized by co-precipitation approach can be significant as well.

2. Experimental

2.1. Materials

All the analytical grade chemicals were used without further modification. The precursors used were copper acetate monohydrate [$Cu(CH_3COO)_2.H_2O$] and urea [CH_4N_2O] where sodium hydroxide [NaOH] was used for pH control. Urea was used as nitrogen source since urea is a cheaper reagent that promotes controlled nucleation and growth of nanocrystals [50]. Glacial acetic acid was added to prevent hydrolysis of copper acetate to $Cu(OH)_2$ in uncontrolled way prior to NaOH addition.

Table 1
List of previous works on photocatalytic performance of CuO NPs [28,33,35–37].

Catalyst	Synthesis Method	Morphology	Pollutant	Degradation rate
CuO	One pot way	Nanoribbon	RhB	92% after 8hr irradiation
Zn doped CuO	Hydrothermal	Nanosheet	Methylene Blue (MB)	66% after 270 min
F doped CuO	Co-precipitation	Spherical	RhB	89%
CuO/CdS nanocomposite	Ultrasound assisted wet-impregnation method	Nanosheet	RhB	93%
Ce doped CuO	Co-precipitation	Nanoleaves	MB	31% after 180 min

2.2. Synthesis of nanoparticles

Stock solution of $Cu(CH_3COO)_2.H_2O$ prepared using deionized (DI) water was stirred at 60 °C and after 10 min, 1 mL glacial acetic acid was added. After 60 min of stirring, NaOH was added dropwise at constant temperature until solution pH was adjusted to 7 and the precipitates obtained were allowed to settle down for next 48 h. Precipitates were separated by centrifuging several times by washing with DI water and finally once with ethanol to remove any undesirable solvent. After drying for 24 h at 120 °C, the samples were grinded, weighed and then annealed at 400 °C for 1 h in a tube furnace. In the case of doped samples, urea **(**CH_4N_2O) was added 20 min after addition of glacial acetic acid and the rest of the procedure was identical.

3. Characterization

3.1. X-ray diffraction (XRD)

XRD was performed to analyze phases present after annealing and to estimate crystallite size as well as crystallinity by using X-ray diffractometer (Rigaku Smart lab® SE) with 0.15406 nm Cu-K_α radiation for Bragg's angle (2θ) range from 20° to 80° (40 kV, 40 mA, step width 0.02, scanning speed 10°/min).

3.2. Field emission scanning electron Microscopy (FE SEM)

Raman Spectroscopy.
Raman spectra was recorded using MacroRam™ Raman Spectrometer with an excitation wavelength of 785 nm.

3.3. X-ray photoelectron spectroscopy (XPS)

The X-ray photoelectron spectra (XPS) were obtained from X-ray photoelectron spectrometer (XPS) using Al K_α (E = 1486.6 eV) radiation to verify the existence of different elements on the surface of NPs. From XPS spectra effect of doping on defects was also investigated.

3.4. Ultraviolet visible (UV–Vis) spectroscopy

Diffuse reflectance spectra (DRS) of the NPs and absorbance for Rh B solution were measured with PerkinElmer Lambda 365 spectrophotometer. From the reflectance spectra band gap was calculated using Kubelka-Munk formula.

3.5. Photoluminescence (PL) spectroscopy

Photoluminescence spectra for all the nanoparticles were recorded using 224 nm excitation wavelength (Mini PL 110, Photon systems).

3.6. Photocatalytic activity Measurement

The photocatalytic activities of pure and N doped CuO NPs were studied using Rh B dye as a probe molecule for photodegradation in aqueous solution under UV light (florescent lamp of 6W power and 365 nm wavelength) irradiation. 3 M solution of sodium

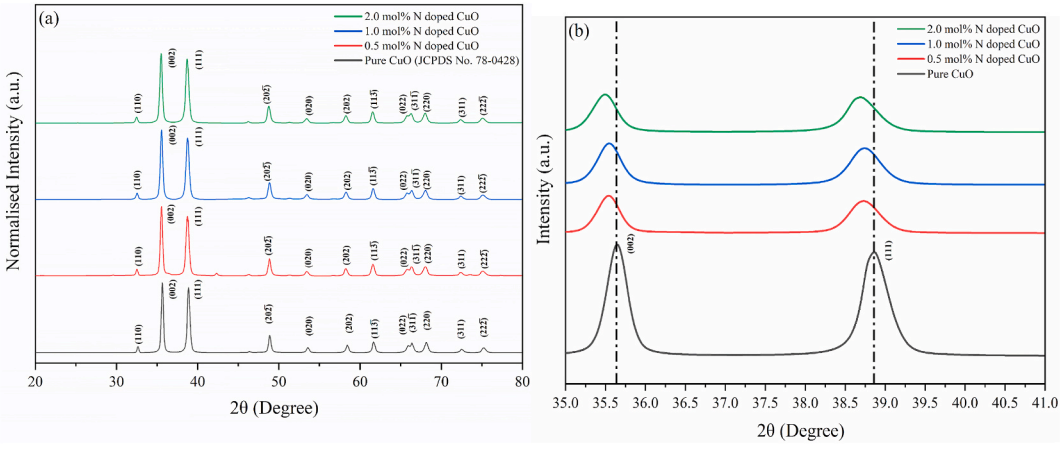

Fig. 1. (a) XRD patterns of pure and N doped CuO NPs, (b) Shift in peak positions after nitrogen doping.

hydroxide was used to maintain pH value at 11. Prior to the episode of UV irradiation, suspension of NPs in Rh B dye was stirred magnetically for 30 min in a dark box to attain the absorption desorption equilibria. The analysis started by extracting 4 mL solution at regular time intervals to measure the degradation under UV light. Each time the sample extracted was centrifuged right away to remove any remaining particles from the solution and absorbance was measured using the UV–Vis spectrometer. Throughout the entire procedure, the pH of the suspension was kept constant. Scavenger test was conducted further to identify the active species involved in degradation process. Degradation efficiency and kinetics of photocatalytic activity were calculated for all the nanoparticles prepared earlier.

4. Results and DISCUSSION

4.1. Structural investigation

X-ray Diffraction (XRD)

Crystal structure with phase identification of pure and N doped CuO NPs were measured by analyzing XRD patterns and the combined XRD patterns are shown in Fig. 1(a). Diffraction peaks were observed for all the samples at 32.64°, 35.64°, 38.86°, 48.88°, 53.45°,58.42°, 61.64°, 65.92°, 66.38°, 68.18°,72.36° and 75.26° which correspond to (110), (002), (111), (20 $\underline{2}$), (020), (202), (11 $\underline{3}$), (022), (31 $\underline{1}$), (220), (311) and (22 $\underline{2}$) planes, respectively [51]. All these data are in well agreement with the standard JCPDS file no.78-0428for monoclinic copper oxide. No extra phase was observed on doping, which indicates complete incorporation of dopants in the CuO lattice [52].

The crystallinity of the pure and N doped NPs is tabulated in Table 2 calculated using this formula:

$$\text{Crystallinity } (\%) = \frac{Areaofcrystallinephase}{TotalArea} \times 100\%$$

The decrease in peak intensity with increasing dopant concentration is evident, implying a subsided crystallinity that can be attributed to the disturbance created in the lattice by dopant incorporation, as shown in Fig. 1(a). The diffraction peaks for the N doped CuO NPs shifted towards a lower 2θ values with an increased peak broadening, indicating the incorporation of nitrogen atoms in the host lattice where N^{3-} ions (ionic radii = 1.71 Å) replace O^{2-} ions (ionic radii = 1.32 Å), creating lattice distortion. The introduction of nitrogen doping caused continuous peak shift in the XRD spectra measuring a decrease of around 0.16° for 2 mol% N doped CuO NPs at (002) and (111) planes shown in Fig. 1(b). The peak broadening can be seen in nitrogen doped samples which might be the reason behind the decreased crystallite size in N doped CuO NPs [53,54]. The decrease in crystallinity was also evident later from the calculated crystallinity (Table 2) [55]. Crystallite size was determined using Debye-Scherrer formula:

$$D(nm) = \frac{K\lambda}{\beta coscos\theta}$$

Where, K is Scherrer constant (0.9), λ is wavelength of Cu K_α radiation (1.54056 nm), β is full width at half maxima (FWHM) of the diffraction peaks and 2θ is Bragg angle [56]. A decrease in crystallite size for the doped NPs may be due to Cu–N–Cu bond formation [57]. It may also be attributed to the controlled crystallization in presence of urea [50,58].

Micro-strain of the pure and N doped CuO NPs was assessed by Williamson-Hall plot (Fig. 2) using following formula:

$$\beta\ cos\ \theta = \frac{\lambda K}{D} + 4\varepsilon\ sin\ \theta$$

This formula depicts a straight line, where ε is slope that gives the lattice strain, λ is wavelength of Cu K_α radiation, K is Scherrer constant, D is crystallite size (nm) and 2θ is Bragg angle [59,60]. The micro-strain of pure CuO NPs was decreased on 0.5 mol% N doping. With initial doping, it is believed that nitrogen fills up the oxygen vacancy of p-type CuO which relaxes the strain of the host lattice. However, for further doping micro-strain increased continuously referring to higher concentration of defects like vacancies [32]. In the lattice, O^{2-} ion was substituted by N^{3-} ion and created a charge imbalance (defect reaction 1). This imbalance of charge compelled three O^{2-} to leave the lattice site which was filled by two N^{3-} ions and leaving an oxygen vacancy that led to increased micro-strain [61,62]. The effect of doping on defects was further studied from PL spectroscopy and XPS analysis later.

$$2N + 3CuO \rightarrow 2N_o^{'} + V_o^{\bullet\bullet} + 3Cu_{Cu}^{x} \quad (1)$$

Table 2
Data analysis of pure and N doped CuO NPs.

Sample	Crystallite Size, D (nm)		Crystallinity (%)	Micro-strain Ɛ (10^{-3})	Particle Size (nm)	Optical Bandgap (eV)
	Debye-Scherrer formula	W–H plot				
CuO	26.21	24.31	84.39	3.77	44.84	1.232
$CuO_{0.995}N_{0.005}$	21.67	22.07	83.88	2.06	–	1.207
$CuO_{0.99}N_{0.01}$	14.64	17.77	80.76	2.92	51.88	1.186
$CuO_{0.98}N_{0.02}$	15.43	18.96	78.53	3.34	75.58	1.212

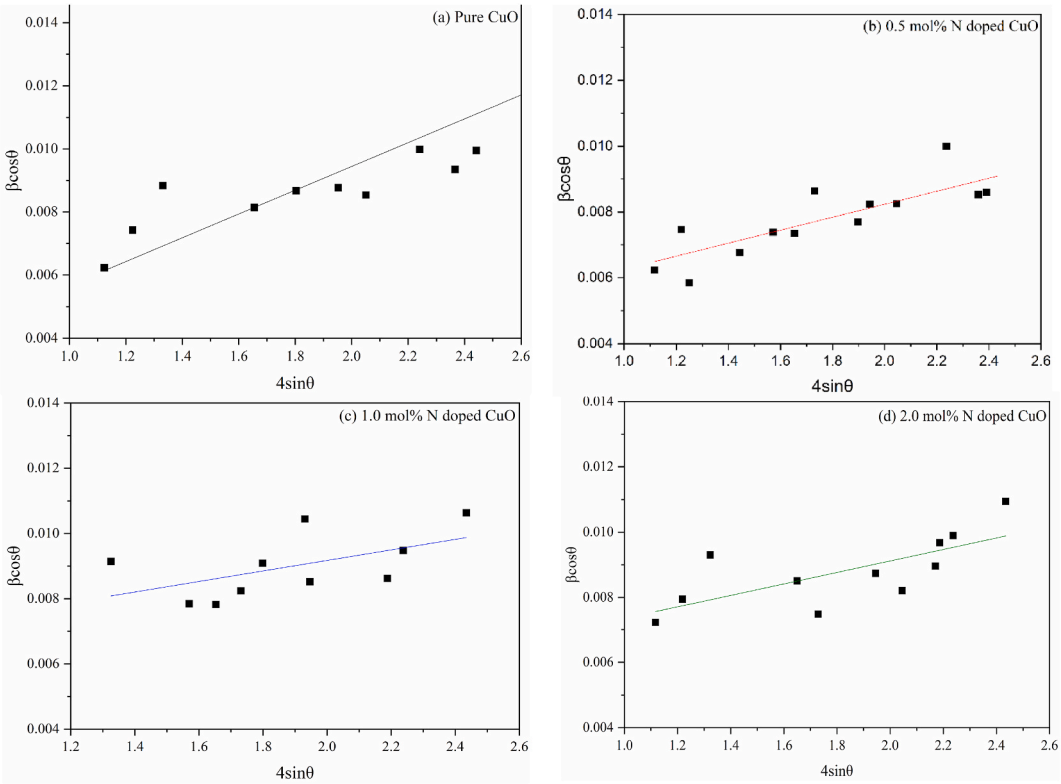

Fig. 2. Williamson-Hall plots of (a) pure, (b) 0.5 mol%, (c) 1.0 mol% and (d) 2.0 mol% N doped CuO NPs.

The above defect reaction is written using Kröger–Vink notation [63]. In this reaction, $N_O^{'}$ refers to the substitution of O^{2-} with N^{3-} creating unit negative charge and $N_O^{\bullet\bullet}$ represents formation of oxygen vacancy of double positive charge. In addition, Cu_{Cu}^{x} represents placement of Cu atom on its own lattice site, and therefore, is neutral.

5. Optical properties

5.1. *Diffusive Reflective spectra analysis*

As it reveals from the diffuse reflectance spectra, reflectance of the NPs in the visible region reduced with increasing dopant

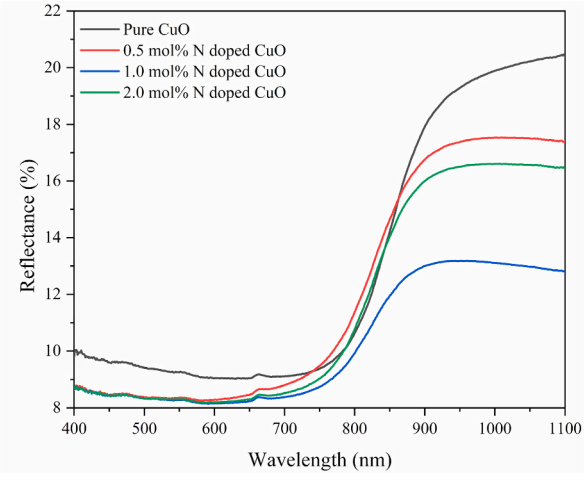

Fig. 3. Diffuse reflectance spectra of pure and N doped CuO NPs.

concentration (Fig. 3). Reflectance was minimum for 1.0 mol % N doped NPs, whereas reflectance increased a bit for further dopant addition. The steep fall of reflectance in DRS spectra for all the CuO samples reflects crystalline nature of the nanoparticles, which is in accord with estimated crystallinity from XRD. Kubelka-Munk formula, as mentioned below, was used to calculate indirect bandgap energies of the nanoparticles.

$$[F(R)h\nu]^n = A\left(h\upsilon - E_g\right)$$

Where $F(R)$ is Kubelka-Munk function, $h\upsilon$ is photon energy, E_g is bandgap and A is a constant.

From $[F(R)h\upsilon]^n$ vs hυ plot indirect bandgap was calculated for all the samples where n takes the value of½ [64,65] (Fig. 4). The indirect bandgap energies of pure, 0.5 mol%, 1.0 mol% and 2.0 mol% N doped CuO nanoparticles were found to be 1.232 eV, 1.207 eV, 1.186 eV and 1.212 eV, respectively.

It is evident that the bandgap initially decreased with addition of N in CuO NPs, but for further doping beyond 1.0 mol% the bandgap was increased. The decrease in bandgap upon N doping can be due to intragap defect states formation [66]. The addition of N^{3-} in the lattice substitute O^{2-} ions and create intermediate N 2p impurity level on top of the valence band (O 2p) of the CuO samples which in turns narrows the bandgap [67]. It has been reported earlier that the bandgap narrowing becomes challenging for higher amount dopant concentration as the valence band and conduction band hardly shift their positions for increased amount dopants Nitrogen-doped simple and complex oxides for photocatalysis [68].

5.2. FTIR analysis

Infrared spectra of pure and 1.0 mol% N doped CuO is illustrated in Fig. 5. The spectra are recorded in the range of 400–4000 cm^{-1}. Here, the FTIR spectrum of pure CuO exhibited characteristic IR peaks at 408, 416 and 589 cm^{-1}, which indicates the presence of monoclinic CuO phase [64,69]. No additional peak of Cu_2O is present in the spectra which confirms the presence of CuO only, as shown by XRD analysis earlier. In addition, minor peaks observed at 1353 and 1494 cm^{-1} indicate carbonyl C═O stretching bonds [69]. For 1.0 mol% N doped CuO NPs, peak at 1401 cm^{-1} corresponds to N–H bending vibration modes and is the characteristic peak for the substitution of N in the CuO NPs [70]. In addition, peak at 3364 cm^{-1} represents O–H vibration stretching mode [70]. In the figure, noticeable shifting and broadening of the characteristic peaks of CuO is seen which indicates the incorporation of N dopant in the NPs

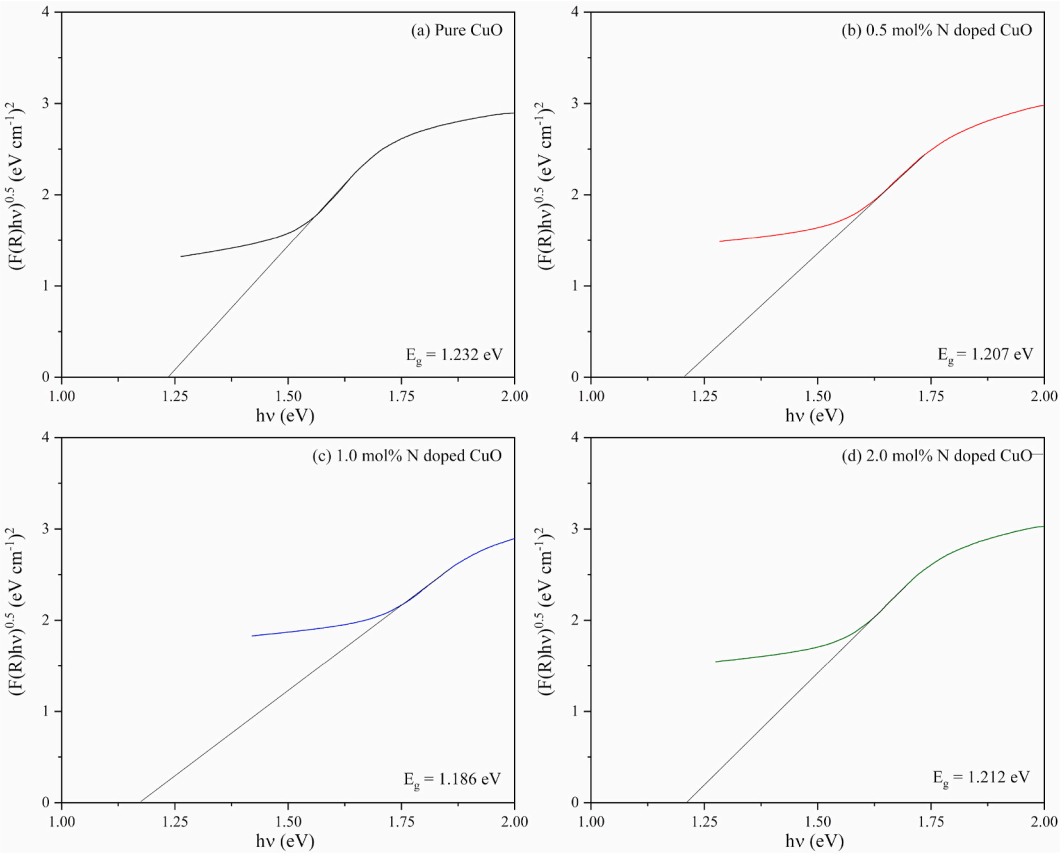

Fig. 4. Indirect optical bandgap of (a) pure, (b) 0.5 mol%, (c) 1.0 mol% and (d) 2.0 mol% N doped CuO NPs.

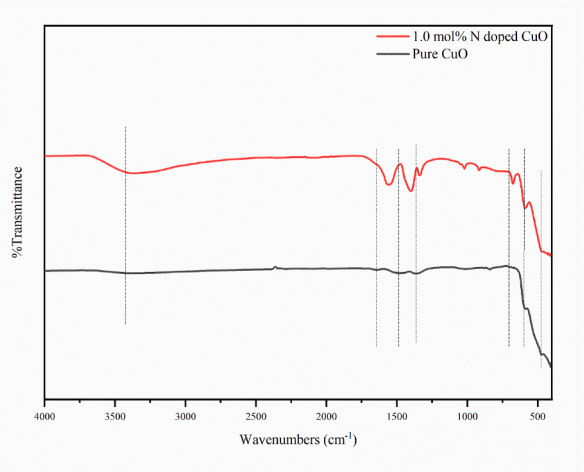

Fig. 5. FTIR spectra of pure CuO and 1.0 mol% N doped CuO NPs.

[71].

5.3. Raman analysis

Raman Spectroscopy was conducted to get further insight into the vibrational properties, change in microstructure prior doping and the defects in the CuO NPs [72].The monoclinic crystal structured CuO belongs to the C_{2h}^{6} (c^2/c) space group, which suggests the presence of twelve zone-center optical phonon modes ($4A_u + 5B_u + A_g + 2B_g$), where only three modes ($A_g + 2B_g$), are Raman active. Due to the lattice site symmetry, transposition of oxygen atoms only attributes to the Raman modes while the Cu atoms remain static for the mentioned phonon modes [73]. Fig. 6 shows the Raman spectra of CuO, and 1.0 mol% N doped CuO NPs, where the observed peaks are in well accord with the previously reported values [74]. The peak with highest intensity appeared at 294 cm^{-1}, A_g mode, refers to the in-phase/out-of-phase rotation of CuO. The other two less intense peaks at 341 and 626 cm^{-1} correspond to the B_g modes which are associated to host lattice (CuO) bending mode and symmetric oxygen stretching, respectively [73]. The absence of any additional Cu_2O related peaks suggests that CuO NPs formed in a single phase in both nitrogen doped and undoped samples corroborating other characterization analysis. All three peaks of the nitrogen doped CuO Nps ($A_g + 2B_g$) shifted towards higher wavenumbers, which might be due to the contraction of the lattice size as the incorporation of nitrogen atoms creates oxygen vacancies in the host lattice for charge neutrality [75]. The crystallite size contraction for 1 mol% N doped CuO NPs is verified by the XRD study, and the emergence of oxygen vacancies is evident from the XPS analysis. Previously, three Raman modes in CuO were thought to be solely caused by oxygen atom vibrations. However, further investigations revealed that any change in Raman modes is related to grain size as well [76].

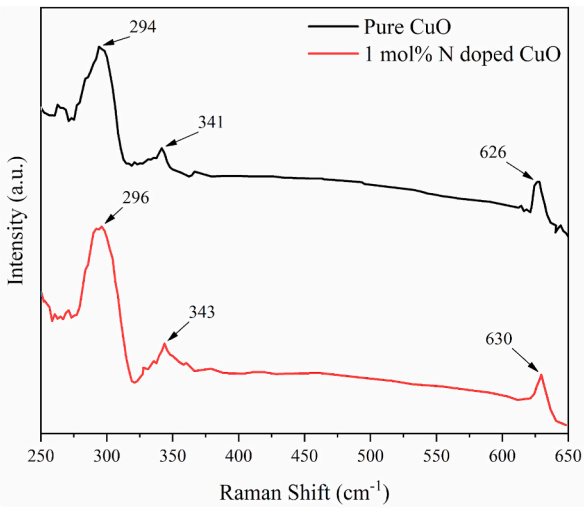

Fig. 6. Raman Spectra of Pure and 1.0 mol% N doped CuO.

5.4. XPS analysis

The characteristic peaks at 933.60 eV, 953.17 eV, and 529.65 eV, which are indicative of binding energies of Cu2p$_{3/2}$, Cu 2p$_{1/2}$, and O 1s confirm the CuO phase in the survey scan of undoped CuO nanoparticles in Fig. 7 (a). N doped CuO nanoparticles exhibited nearly identical binding energies for Cu2p$_{3/2}$, Cu 2p$_{1/2}$, and O 1s, which are at 933.48 eV, 953.36 eV, and 529.50 eV as shown in Fig. 7 (b). The C1s peak observed at 284.78 eV in both general survey scans was used as a reference [29]. High resolution scanning confirmed the presence of N 1s at 400.4 eV in the doped nanoparticles depicted in Fig. 8(b).

The C 1s spectra was further resolved into four distinct peaks to understand the chemical states of carbon present in the survey scans illustrated in Fig. 8(a). The peak associated to C–C bond was located at 284.78 eV [29]. Other peaks observed at 283.57 eV, 287.4 eV and 289.96 eV represent the metal carbide, C–H bond and CO_3 respectively [77].

Fig. 9(a) exhibits the core spectra of Cu 2p for pure CuO nanoparticles which appeared as a doublet associated with satellite peaks. The peaks observed in pure CuO at 933.6 eV and 953.52 eV resemble binding energies of Cu 2p$_{3/2}$ and Cu 2p$_{1/2}$ with a spin orbit separation of 19.92 eV and extra satellite peaks resemble these two peaks appeared at 941.23 eV and 962.06 eV with a separation of around 20.83 eV. Again, the Cu 2p spectra for the N doped nanoparticles appeared with nearly identical binding energies for Cu 2p$_{3/2}$ (933.50 eV) and Cu 2p$_{1/2}$ (953.55 eV) with a spin orbit separation of 20.05 eV in Fig. 9(b). The satellite peaks associated with Cu 2p$_{3/2}$ and Cu 2p$_{1/2}$ in the N doped CuO are found at 941.15 eV and 962.05 eV with an energy gap of 20.9 eV. The existence of the ionic state Cu^{2+} was confirmed in both nanoparticles by the peaks that originated from the core level of Cu 2p as well as the shake-up satellite peaks [37,78]. Fig. 8 (b) depicts core XPS spectra for N 1s state at 400.4 eV which supports the previous claim of the formation of nitrogen-Copper bond by successful incorporation of nitrogen ions in CuO nanoparticles [79].

Amounts of oxygen ions at lattice sites and oxygen vacancies were calculated for all the nanoparticles by performing deconvolution of the peaks (Fig. 10). In Fig. 10 (a), deconvolution of O 1s for undoped NPs showed two individual fitted peaks at 529.62 eV and 531.27 eV. Former peak represents oxygen ions at the lattice points and the latter one corresponds to the oxygen vacancies [37,80]. Peaks found from deconvolution of O 1s for the nitrogen doped NPs were at 529.55 eV and 531.05 eV (Fig. 10 (b)). Amount of oxygen ions at lattice sites and the amount of oxygen vacancies were estimated from the area under their relevant peaks which were around 51.15% and 48.85 % for pure CuO and around 48.93% and 51.07% for the N doped CuO resulting in about 2.22% increase in the oxygen vacancies on doping. The increase in the oxygen vacancies is attributed to N^{3-} settling at the oxygen lattice sites and forming new vacancies to maintain charge balance described in defect reaction (1) [48], [65]. This phenomenon is also supported by the strain analysis in XRD analysis and further confirmed by PL analysis discussed later.

5.5. Morphological analysis

The morphology of all the NPs were studied using FE SEM (Fig. 11) and the particle size distributions are shown in Fig. 12. Pure CuO NPs were found to be spherical and on doping particle shape showed significant deviation from spherical shape [81,82]. For 0.5 mol% N doping, nanoparticles became agglomerated and formed large cauliflower-like structure. Such morphology with large surface area and short conduction length for electrons and cations are suitable for electrochemical reactions [55,83]. Due to agglomeration, particle size distribution could not be measured for 0.5 mol% N doping. Further doping caused the evolution of particles with larger average particle size and wider particle size distribution compared to pure CuO. Average particle size for pure, 1.0 mol% and 2.0 mol% N doped CuO NPs are found to be 44.84 nm, 51.89 nm, and 71.59 nm, respectively.

5.6. Photoluminescence studies

The photoluminescence (PL) spectra were recorded for all the nanoparticles to study the effect of dopants on the resulted defects on doping (Fig. 13). For PL spectroscopy the stimulation wavelength was 224 nm. After the second order artefacts with a Rayleigh scatter

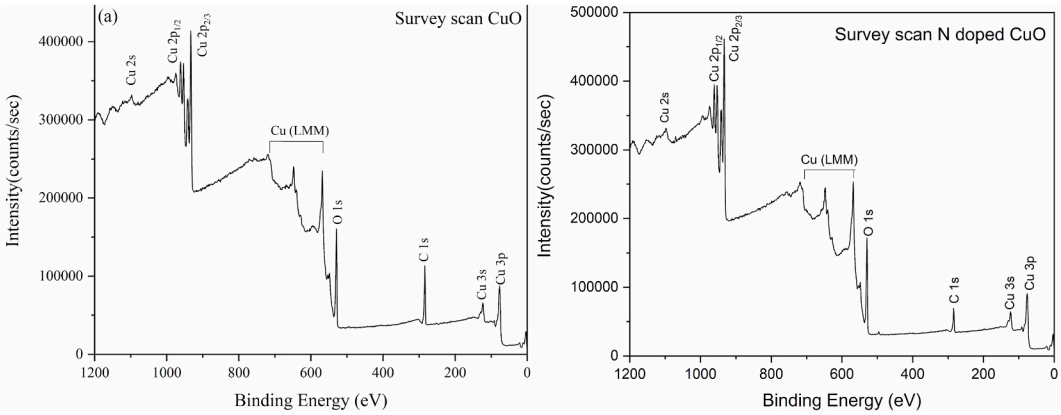

Fig. 7. Survey scan of (a) Pure and (b) 1.0 mol% N doped CuO.

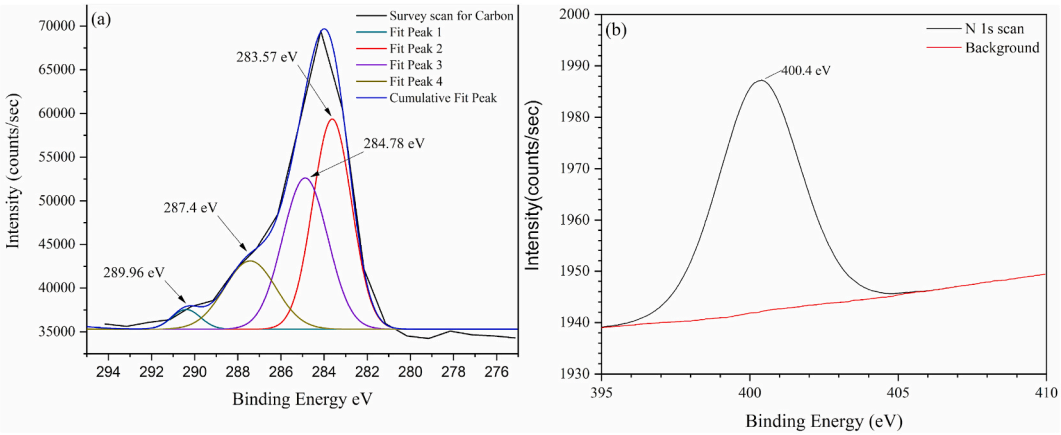

Fig. 8. Core level XPS spectra for (a) C-1s spectrum (b) N 1s of 1.0 mol% N doped CuO NPs.

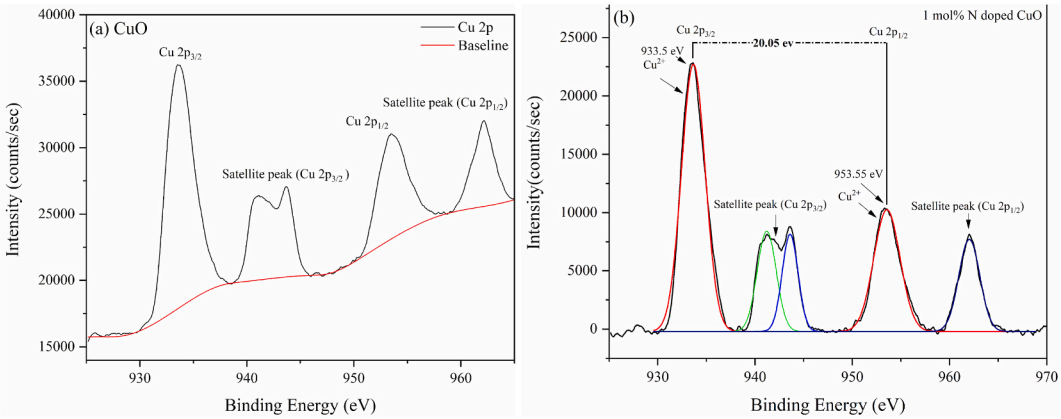

Fig. 9. Core level XPS spectra for Cu 2p of (a) pure and (b) 1.0 mol% N doped CuO.

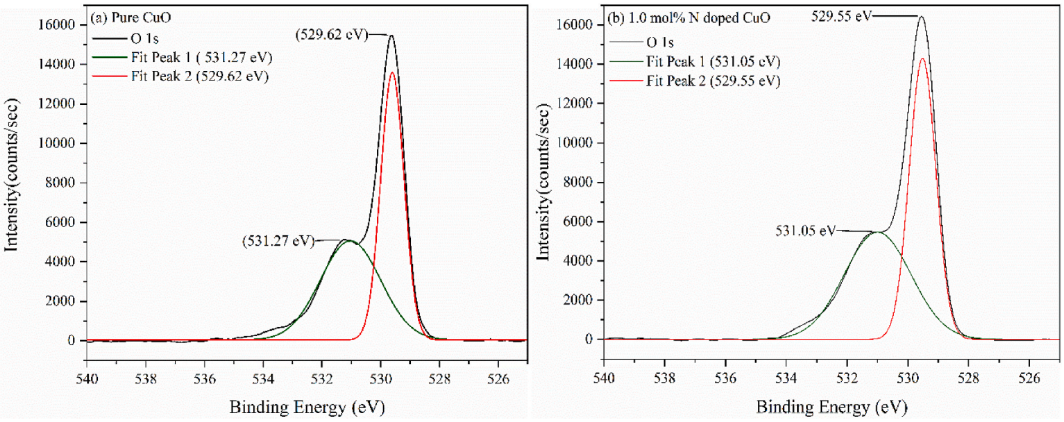

Fig. 10. XPS spectra for O 1s in (a) pure (b) 1.0 mol% N doped CuO.

peak at 448 nm, deep band emissions (DBE) were observed. The blue emission peak at 471 nm can be due to transition of oxygen vacancy and interstitial oxygen [84]. The green emissions at 512 and 533 nm correspond to electron-hole recombination at oxygen vacancies [67]. Oxygen vacancies are created on doping as predicted by defect reaction (1) mentioned earlier. The intensity of deep band emissions varied with increasing doping concentration. Intensity of these peaks decreased for doping concentration up to 1.0 mol % which implies reduced recombination rate of excitons due to effective trapping by the defects induced by nitrogen doping [57].

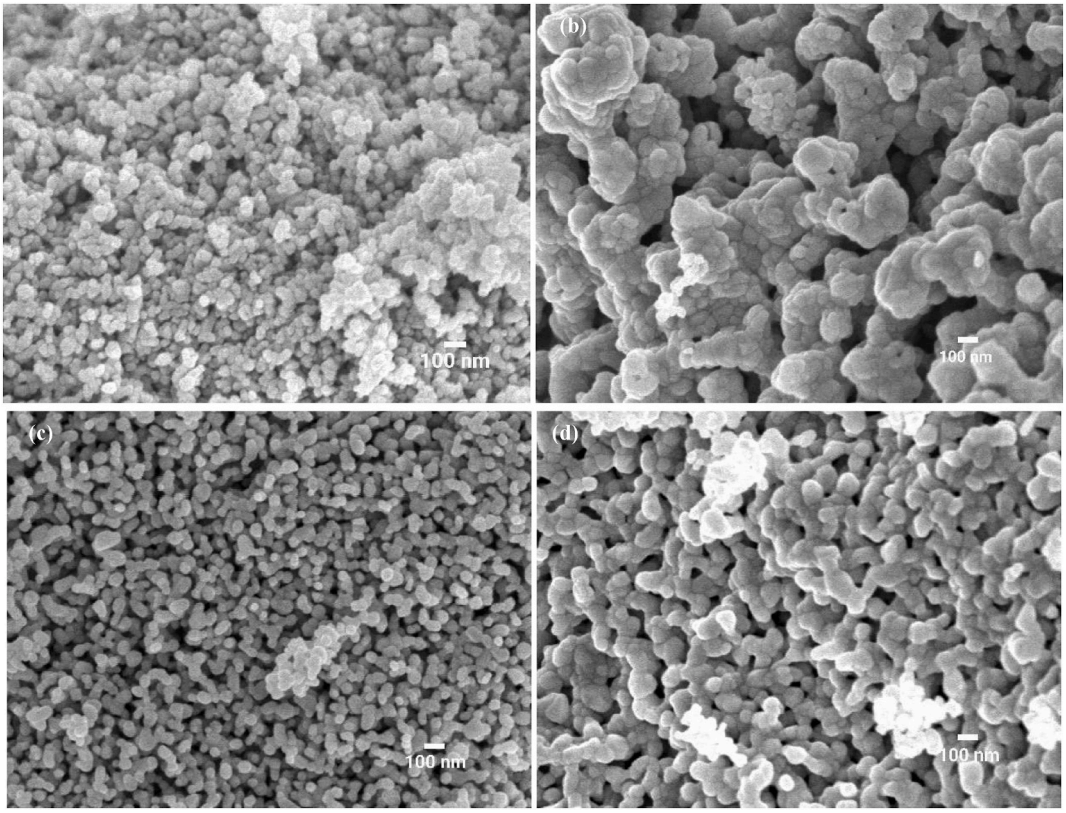

Fig. 11. FE SEM images of (a) Pure, (b) 0.5 mol%, (c) 1.0 mol% and (d) 2.0 mol% N doped CuO NPs.

However, on further doping a slightly increased recombination rate was noticed evident from enhanced peak intensity. Reasons can be defect annihilation, or because the defects started to act as exciton collapse center for 2.0 mol% N doping or the larger particle size (Fig. 11 (d)) as for large exciton collapse takes place prior to particle surface enrichment with charge carriers [85,86].

6. Photocatalytic degradation

6.1. Degradation efficiency and kinetics

Fig. 14 shows the absorption spectra of Rh B with time to study the photocatalytic degradation effect of undoped and doped CuO NPs after adding in the dye under UV light. Here, the intense peak of Rh B at 560 nm decreased significantly under UV irradiation at a steady rate. For all the doped samples, the decrease in absorbance intensity was faster than pure CuO. After 6 h of irradiation, pure CuO nanoparticles showed degradation of 79% whereas 0.5 mol%, 1.0 mol% and 2.0 mol% N doped CuO nanoparticles showed degradation of 88%, 94% and 91%, respectively (Fig. 15(a)). This implies that with increased doping, degradation increased up to 1.0 mol% N doping and then reduced with further doping. Degradation efficiency was estimated from the formula:

Degradation efficiency (%) $\frac{A_o - A}{A_o} \times 100\% = \frac{C_o - C}{C_o} \times 100\%$ [87]

Where C_O, C, A_o and A refer to initial concentration of dye, final concentration of dye, absorbance before and after dye degradation respectively. The reason for the lower degradation of pure CuO might be the faster recombination of charge carriers, which could restrict the movement of the photogenerated charge carrier at catalysts surface and resulted inferior photocatalytic performance [88].

The kinetic parameters were calculated using the first-order kinetics equation as below and $ln\frac{C_o}{C}$ vs t diagram (Fig. 15(b)) was plotted using OriginPro software for all the samples:

$$ln\frac{C_o}{C} = Kt$$

Where, K is the first-order rate constant. Values of K were determined from slope of the lines and the calculated values were 0.26337 hr^{-1}, 0.35574 hr^{-1}, 0.44218 hr^{-1} and 0.38559 hr^{-1} for pure CuO, 0.5 mol%, 1.0 mol% and 2.0 mol% N doped CuO nanoparticles, respectively. Here, the maximum value was obtained for 1.0 mol% N doped CuO nanoparticles sample. From Fig. 14, it is evident that absorption of the nanoparticles increased after N doping, which led to higher photocatalytic efficiency of the doped nanoparticles. This enhanced absorption can be attributed to the change of CuO electronic structure due to N dopant [8]. Additionally,

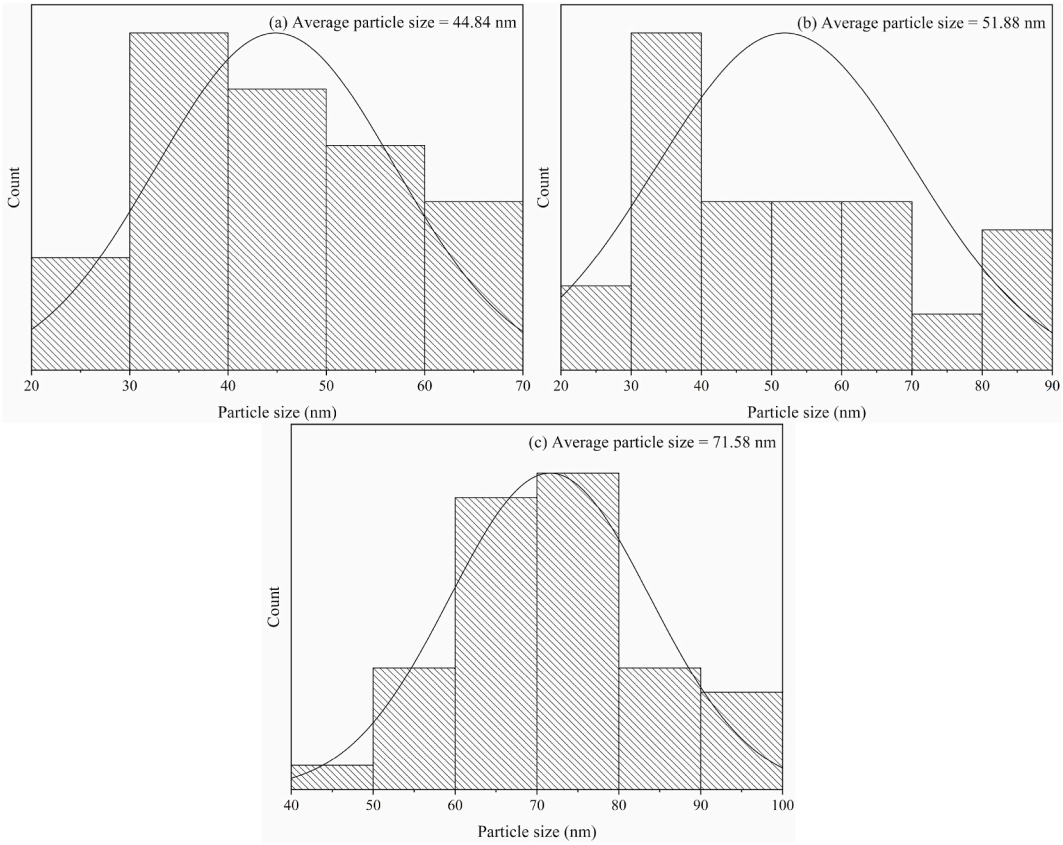

Fig. 12. Particle size distribution of (a) pure, (b) 1.0 mol% and (c) 2.0 mol% N doped CuO NPs.

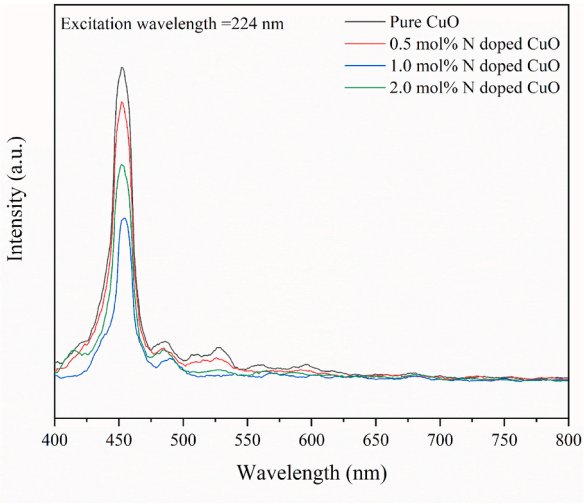

Fig. 13. PL emission spectra showing deep band emission (DBE) of pure and N doped CuO NPs.

compared to pure CuO, the N doped CuO nanoparticles had lower band gap up to 1.0 mol% doping as particle size increased. 1.0 mol% N doped CuO nanoparticles showed maximum degradation rate which can be due to the minimum exciton collapse rate as observed from the photoluminescence study. As discussed earlier, the intra-band gap sideway defect states reduced the band gap on doping and believed to decrease recombination rate of excitons by effective trapping. Initially exciton recombination and trapping rate, and later recombination and the interfacial charge transfer rate determines overall quantum efficiency of the charge transfer [89]. Another reason for the higher degradation rate of 1.0 mol% N doped CuO might be higher concentration of oxygen vacancies. Because with

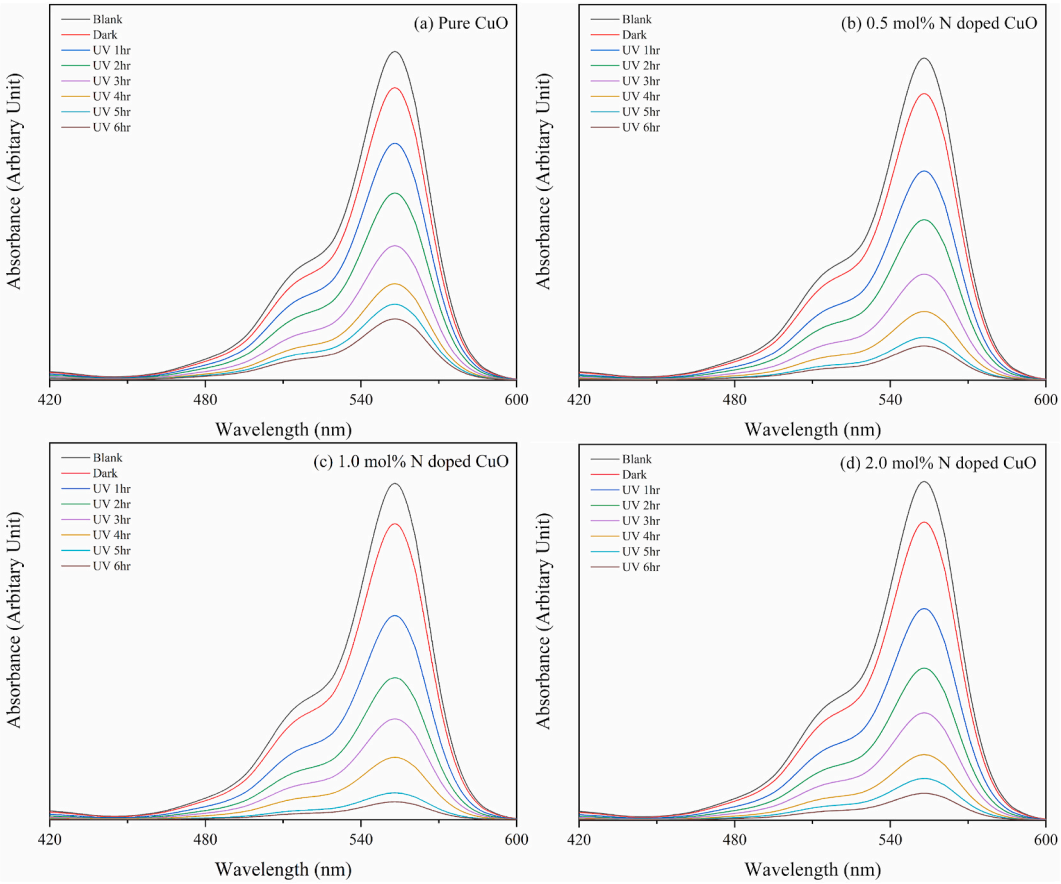

Fig. 14. Absorption spectra of Rh B solution after (a) pure, (b) 0.5 mol%, (c) 1.0 mol% and (d) 2.0 mol% CuO NPs addition under UV irradiation.

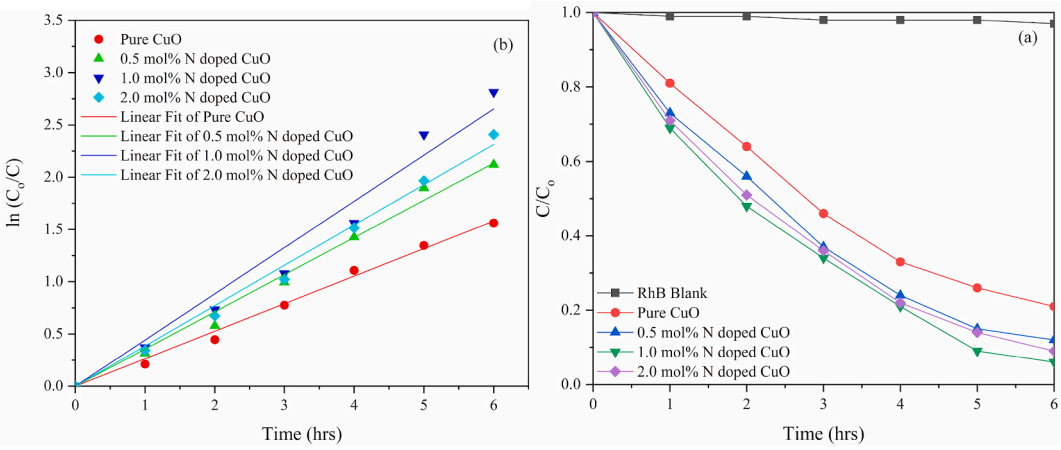

Fig. 15. (a) Degradation curves and (b) kinetics of photocatalytic activity of pure and N doped CuO NPs.

larger oxygen vacancy content, charge carrier recombination rate reduces. This also implies that lower recombination rate is the reason for greater amount of degradation [88]. However, reduced photocatalytic activity was noticed for 2.0 mol% N doping can be due to the thin space layer which makes recombination rate easier and lowers degradation efficiency [90]. Also, photoluminescence study showed an increased recombination rate of excitons for 2.0 mol% N doping which caused the decreased photocatalytic activity for this higher doping concentration.

6.2. Active species for photocatalytic degradation

The effects of different scavengers in the degradation of photocatalysts were analyzed by comparing the inhibiting effect of each active species on the degradation efficiency of photocatalysts. Generally, hydroxyl radical (OH·), superoxide radical ($O_2\cdot^-$), holes (h^+) and electrons (e^-) act as active species in photocatalytic degradation of Rh B and isopropyl alcohol (IPA) [91], ascorbic acid (AA) [92], sodium chloride (NaCl) [93] and sodium nitrate ($NaNO_3$) act as scavengers of these species respectively. Fig. 16. (a) and (b) illustrate the individual influence of these trapping agents, where isopropyl alcohol (IPA) exhibits noticeable inhibition effect in comparison to the rest of scavengers. From the results, it is evident that hydroxyl radical (OH·) plays the role of major reactive species since isopropyl alcohol (IPA) reduces the degradation efficiency of Rh B from 94% to 4.52%. The figure also depicts that, with hydroxide radicals (OH·), superoxide species ($O_2\cdot^-$) contribute to the photocatalytic degradation.

6.3. Mechanism

The degradation mechanism of photocatalysts was speculated after integrating several related articles[94] and is illustrated in Fig. 17 [57], [87], [92], [94], [95]. When irradiated with UV light, excited electrons ($e^-_{(cb)}$) from valence band transferred to conduction band creating positive holes ($h^+_{(vb)}$) in valence band. This jump of electrons results in generation of large number of hydroxyl species (OH·) and superoxide species ($O_2\cdot^-$). The excited electrons ($e^-_{(cb)}$) of conduction band produce negatively charged superoxide radicals ($O_2\cdot^-$) by interacting with oxygen, which later produce hydroxyl radicals (OH·). Also, reaction of H^+ and superoxide species ($O_2\cdot^-$) forms hydroperoxyl radical ($HO_2\cdot$). In addition, a sub energy level above the valence band of CuO nanoparticles was introduced due to N doping [95]. This sub energy level traps the generated electrons and holes, and eventually, inhibits electron hole recombination. Adsorbed hydroxide ions on the surface of catalyst generate hydroxyl radicals (OH·) by participating in oxidation reaction with holes ($h^+_{(vb)}$). The entire degradation mechanism can be shown as below

$$CuO + h\nu \rightarrow CuO\left(e^{-+h^+_{(vb)}}_{(cb)}\right.$$

$$O_2 + e^-_{(cb)} \rightarrow O_2\cdot^-$$

$$O_2\cdot^- + H^+ \rightarrow HO_2\cdot$$

$$HO_2\cdot + H^+ + e^-_{(cb)} \rightarrow H_2O_2$$

$$H_2O_2 + e^-_{(cb)} \rightarrow OH\cdot + OH^-$$

$$H_2O + h^+_{(vb)} \rightarrow H^+ + OH\cdot$$

$$OH^- + h^+_{(vb)} \rightarrow OH\cdot$$

$$OH\cdot + \text{Rh B contaminant} \rightarrow \text{Degradation product}$$

6.4. Recyclability study

CuO NPs, as heterogeneous photocatalysts, have excellent capability to demonstrate phase stability after several cycles of the dye

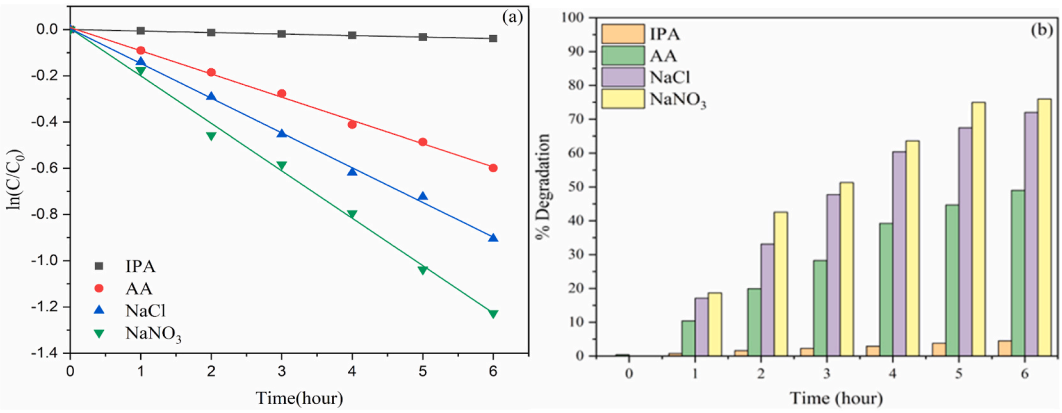

Fig. 16. Effect of different scavengers, (a) ln ($\frac{C}{C_o}$ vs time (b) % Degradation.

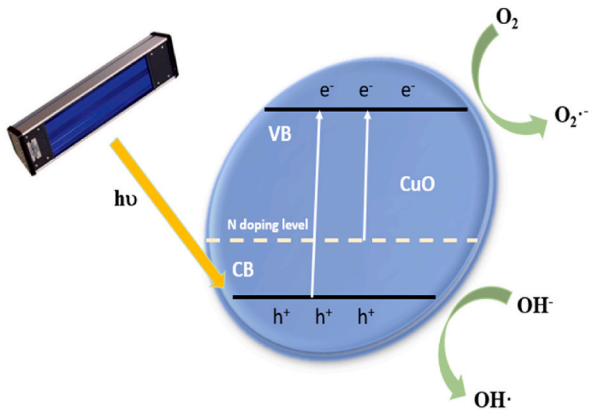

Fig. 17. Photocatalytic degradation mechanism of N doped CuO nanoparticles.

degradation process. In this study, 1 mol% N doped CuO NPs were taken to investigate phase stability, as it showed maximum degradation potency for Rh B dye removal. The nanocatalysts were utilized for four cycles where particles were collected after each cycle, centrifuged thoroughly and then dried in the oven for 1 h. Then the cycle was repeated against a freshly prepared Rh B solution. Fig. 18 (a) illustrates the recyclability of 1 mol% N doped CuO NPs after several use. The dye removal efficiency was approximately 93% after the 1st cycle in 6 h of UV light irradiation, which was found to be 89% after the 4th cycle, showed in Fig. 18 (b). The reduction in efficiency may be caused by the unintended loss of catalysts during recovery steps each time. To verify the phase stability, XRD and reflectance spectra were recorded before using the catalysts for photoreaction and after the 4th cycle separately. Fig. 19 (a) shows the identical XRD spectra which strongly confirms the stable monoclinic phase of the N doped CuO NPs after repeated photocatalytic degradation. Moreover, Fig. 19 (b) shows the sharp slope of the reflectance spectrum for the photocatalysts remaining unaltered after successive use, depicting the photo-stability of the synthesized nanoparticles.

7. Conclusion

Here, pure and nitrogen doped CuO NPs have been prepared following co-precipitation route. Structural, morphological, optical and photocatalytic properties of the particles were investigated systematically. Successful incorporation of nitrogen in the CuO lattice was confirmed by XPS, FT-IR and Raman spectra. All the particles synthesized showed single phase CuO with spherical or near spherical morphology with well crystallinity. On doping, band gap decreased up to 1.0 mol% N doping for which recombination rate of excitons was also minimum. 1.0 mol% N doped CuO exhibited maximum photocatalytic degradation efficiency which can be due to the minimum recombination rate of excitons. This can also be due to formation of greater concentration of oxygen vacancies to maintain charge neutrality, as confirmed by XPS and PL studies. For higher dopant concentration, degradation efficiency was decreased due to increased recombination rate caused by defect annihilation, or since defects started to act as recombination center or because of larger particle size. Since N doped CuO NPs exhibit enhanced photocatalytic degradation of organic dye Rh B, it can be used as an effective photocatalyst in wastewater management and hydrogen production [96].

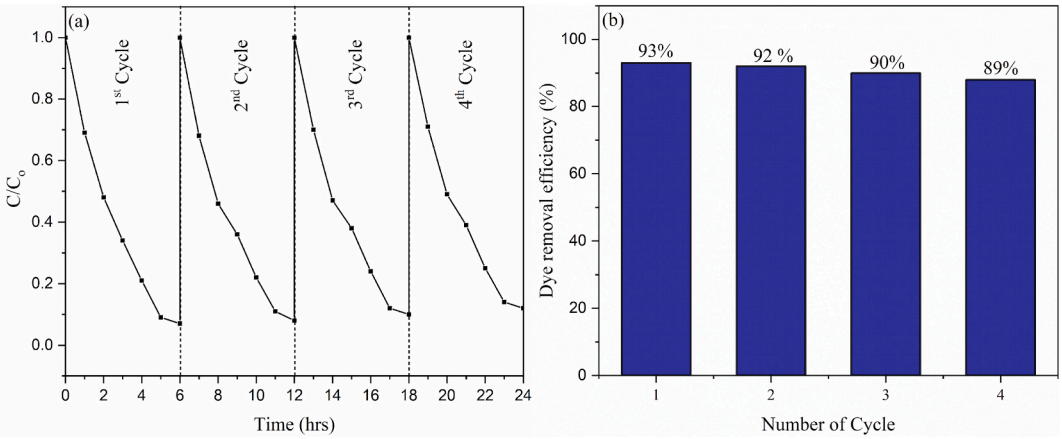

Fig. 18. (a) Recylability of 1 mol% N doped CuO NPs, (b) Dye removal efficiency at successive cycles.

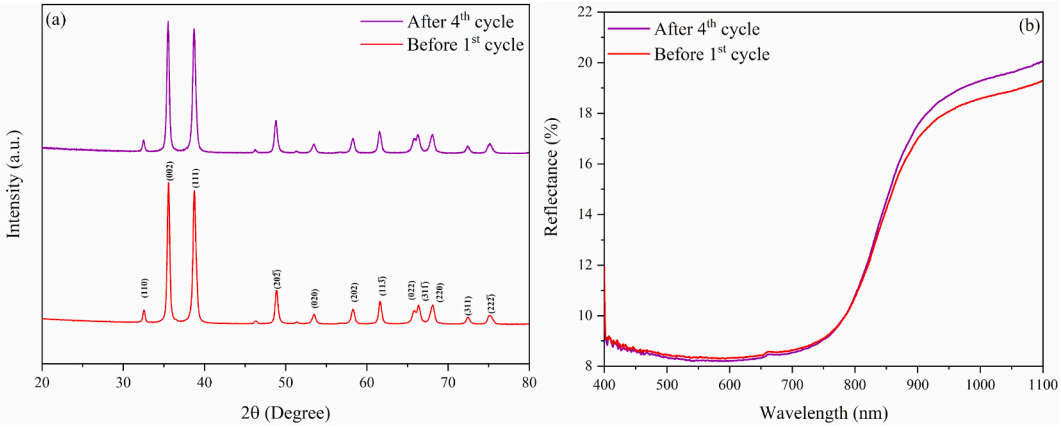

Fig. 19. (a) XRD and (b) DRS spectra of 1 mol% N doped CuO NPs before and after photocatalytic degradation.

CRediT authorship contribution statement

Md Jannatul Ferdous Anik: Writing – original draft, Methodology, Investigation, Formal analysis. **Samiya Rahman Mim:** Writing – original draft, Methodology, Investigation, Formal analysis. **Syed Sammo Swapno:** Writing – original draft, Methodology, Investigation, Formal analysis. **Sirajum Munira:** Writing – original draft, Methodology, Investigation, Formal analysis. **Oishy Roy:** Writing – review & editing. **Md Muktadir Billah:** Writing – review & editing, Supervision, Resources, Funding acquisition, Formal analysis, Conceptualization.

Declaration of competing interest

The authors declare that they have no known competing financial interests or personal relationships that could have appeared to influence the work reported in this paper.

Acknowledgements

This work was funded by the Committee of Advanced Studies and Research (CASR) and funded by the Department of Materials and Metallurgical Engineering (MME), Bangladesh University of Engineering and Technology (BUET).

References

JSM-, 7600F A JEOL JSM-7600F field emission scanning electron microscope (FE SEM) was used for morphology study of the pure and N doped CuO NPs. To calculate particle size, ImageJ software was used, and particle size distribution histogram was obtained using OriginPro 2018.Fig. 2. Williamson-Hall plots of (a) pure, (b) 0.5 mol%, (c) 1.0 mol% and (d) 2.0 mol% N doped CuO NPs.

[1] H. Kumari, et al., "A review on photocatalysis used for wastewater treatment: dye degradation," water, Air, and Soil pollution, Institute for Ionics 234 (6) (2023), https://doi.org/10.1007/s11270-023-06359-9. Jun. 01.
[2] G. Crini, E. Lichtfouse, Advantages and disadvantages of techniques used for wastewater treatment, Environ. Chem. Lett. 17 (1) (2019) 145–155, https://doi.org/10.1007/s10311-018-0785-9. Springer Verlag.
[3] Y. Pi, et al., Adsorptive and photocatalytic removal of Persistent Organic Pollutants (POPs) in water by metal-organic frameworks (MOFs), Chem. Eng. J. 337 (2018) 351–371, https://doi.org/10.1016/j.cej.2017.12.092. Elsevier B.V.
[4] S.N. Ahmed, W. Haider, Heterogeneous photocatalysis and its potential applications in water and wastewater treatment: a review, Nanotechnology 29 (34) (2018), https://doi.org/10.1088/1361-6528/aac6ea. Institute of Physics Publishing, Jun.
[5] Y. Feng, et al., Research progress of graphene oxide-based magnetic composites in adsorption and photocatalytic degradation of pollutants: a review, Mater. Res. Bull. 162 (Jun. 2023) 112207, https://doi.org/10.1016/J.MATERRESBULL.2023.112207.
[6] D. Dodoo-Arhin, et al., Synthesis of nanostructured cupric oxide for visible light assisted degradation of organic wastewater pollutants, Cogent Eng 8 (1) (2021), https://doi.org/10.1080/23311916.2021.1920563.
[7] S. Mondal, S.A. Ayon, M.S. Islam, M.S. Rana, M.M. Billah, Morphological evaluation and boosted photocatalytic activity of N-doped ZnO nanoparticles prepared via Co-precipitation method, Heliyon 9 (10) (Oct. 2023) E20948, https://doi.org/10.1016/j.heliyon.2023.e20948.
[8] Y. Liu, X. Chen, J. Li, C. Burda, Photocatalytic degradation of azo dyes by nitrogen-doped TiO2 nanocatalysts, Chemosphere 61 (1) (2005) 11–18, https://doi.org/10.1016/j.chemosphere.2005.03.069.
[9] S. Rehman, R. Ullah, A.M. Butt, N.D. Gohar, Strategies of making TiO2 and ZnO visible light active, J. Hazard Mater. 170 (2–3) (2009) 560–569, https://doi.org/10.1016/j.jhazmat.2009.05.064. Oct. 30.
[10] X. Chen, S.S. Mao, Titanium dioxide nanomaterials: synthesis, properties, modifications and applications, Chem. Rev. 107 (7) (Jul. 2007) 2891–2959, https://doi.org/10.1021/cr0500535.
[11] J. Pan, H. Shen, S. Mathur, One-dimensional SnO 2 nanostructures: synthesis and applications, Journal of Nanotechnology (2012), https://doi.org/10.1155/2012/917320.
[12] A. Singh, S. Kumar, Study of pure and Ag-doped TiO2nanoparticles for photocatalytic degradation of methylene blue, in: IOP Conference Series: Materials Science and Engineering, IOP Publishing Ltd, Jan, 2021, https://doi.org/10.1088/1757-899X/1033/1/012050.
[13] S. Kumar, A. Kumar, T. Malhotra, S. Verma, Characterization of structural, optical and photocatalytic properties of silver modified hematite (α-Fe2O3) nanocatalyst, J. Alloys Compd. 904 (May 2022) 164006, https://doi.org/10.1016/J.JALLCOM.2022.164006.

[14] S. Mondal, S.A. Ayon, M.M. Billah, Comparative study of structural, optical, and photocatalytic properties of ZnO synthesized by chemical coprecipitation and modified sol–gel methods, Surf. Interface Anal. 55 (6–7) (Jun. 2023) 424–429, https://doi.org/10.1002/sia.7210.

[15] P. Kumar, et al., Surface, optical and photocatalytic properties of Rb doped ZnO nanoparticles, Appl. Surf. Sci. 514 (2020), https://doi.org/10.1016/j.apsusc.2020.145930.

[16] B. Wang, et al., "Improvement in Recycling Times and Photodegradation Efficiency of Core-Shell Structured Fe O @C-TiO Composites by pH Adjustment 3 4 2,", 2019, https://doi.org/10.30919/esmm5f.

[17] V. Vaiano, M. Matarangolo, J.J. Murcia, H. Rojas, J.A. Navío, M.C. Hidalgo, Enhanced photocatalytic removal of phenol from aqueous solutions using ZnO modified with Ag, Appl. Catal., B 225 (Jun. 2018) 197–206, https://doi.org/10.1016/j.apcatb.2017.11.075.

[18] J. Liu, P. Wang, W. Qu, H. Li, L. Shi, D. Zhang, Nanodiamond-decorated ZnO catalysts with enhanced photocorrosion-resistance for photocatalytic degradation of gaseous toluene, Appl. Catal., B 257 (2019), https://doi.org/10.1016/j.apcatb.2019.117880. Nov.

[19] S. Vasantharaj, et al., Synthesis of ecofriendly copper oxide nanoparticles for fabrication over textile fabrics: characterization of antibacterial activity and dye degradation potential, J. Photochem. Photobiol., B 191 (Feb. 2019) 143–149, https://doi.org/10.1016/j.jphotobiol.2018.12.026.

[20] A. Sharma, R.K. Dutta, A. Roychowdhury, D. Das, A. Goyal, A. Kapoor, Cobalt doped CuO nanoparticles as a highly efficient heterogeneous catalyst for reduction of 4-nitrophenol to 4-aminophenol, Appl. Catal. Gen. 543 (2017) 257–265, https://doi.org/10.1016/j.apcata.2017.06.037.

[21] N. 'Gautam, R. 'Abhilasha, "Impact of Bimetal Doping on the Structural and Optical Characteristics of Copper Oxide Nanoparticles to Enhance Photocatalytic Degradation of Dyes: an Investigative Study ".

[22] S.B. Wang, et al., A CuO nanowire infrared photodetector, Sens Actuators A Phys 171 (2) (Nov. 2011) 207–211, https://doi.org/10.1016/j.sna.2011.09.011.

[23] J.C. Park, J. Kim, H. Kwon, H. Song, Gram-scale synthesis of Cu2O nanocubes and subsequent oxidation to CuO hollow nanostructures for lithium-ion battery anode materials, Adv. Mater. 21 (7) (Feb. 2009) 803–807, https://doi.org/10.1002/adma.200800596.

[24] K.J. Choi, H.W. Jang, One-dimensional oxide nanostructures as gas-sensing materials: review and issues, Sensors 10 (4) (Apr. 2010) 4083–4099, https://doi.org/10.3390/s100404083.

[25] J. Liu, et al., Tailoring CuO nanostructures for enhanced photocatalytic property, J. Colloid Interface Sci. 384 (1) (Oct. 2012) 1–9, https://doi.org/10.1016/j.jcis.2012.06.044.

[26] K. Zhou, R. Wang, B. Xu, Y. Li, Synthesis, characterization and catalytic properties of CuO nanocrystals with various shapes, Nanotechnology 17 (15) (2006) 3939–3943, https://doi.org/10.1088/0957-4484/17/15/055. Aug.

[27] S. Anandan, S. Yang, Emergent methods to synthesize and characterize semiconductor CuO nanoparticles with various morphologies - an overview, Journal of Experimental Nanoscience, Mar. (2007) 23–56, https://doi.org/10.1080/17458080601094421.

[28] X. Zhang, et al., Different CuO nanostructures: synthesis, characterization, and applications for glucose sensors, J. Phys. Chem. C 112 (43) (Oct. 2008) 16845–16849, https://doi.org/10.1021/jp806985k.

[29] P. Kumar, G.K. Inwati, M.C. Mathpal, S. Ghosh, W.D. Roos, H.C. Swart, Defects induced enhancement of antifungal activities of Zn doped CuO nanostructures, Appl. Surf. Sci. 560 (2021), https://doi.org/10.1016/j.apsusc.2021.150026.

[30] N.C. Joshi, P. Gururani, S.P. Gairola, Metal oxide nanoparticles and their nanocomposite-based materials as photocatalysts in the degradation of dyes, Biointerface Research in Applied Chemistry 12 (5) (2022) 6557–6579, https://doi.org/10.33263/BRIAC125.65576579. AMG Transcend Association.

[31] X. Zhang, et al., The effect of Ag atom doped Cu@CuO core–shell structure on its electronic properties and catalytic performance: a first principles study, Nanotechnology 32 (2021).

[32] N.M. Basith, J.J. Vijaya, L.J. Kennedy, M. Bououdina, Structural, morphological, optical, and magnetic properties of Ni-doped CuO nanostructures prepared by a rapid microwave combustion method, Mater. Sci. Semicond. Process. 17 (2014) 110–118, https://doi.org/10.1016/j.mssp.2013.09.013.

[33] T.R. Seling, et al., Transition Metal-Doped CuO Nanosheets for Enhanced Visible-Light Photocatalysis, J. Photochem. Photobiol. A: Chem. 448 (2024), https://doi.org/10.1016/j.jphotochem.2023.115356.

[34] K. Shaheen, et al., Metal oxides nanomaterials for the photocatalytic mineralization of toxic water wastes under solar light illumination, Journal of Water Process Engineering 34 (2020), https://doi.org/10.1016/j.jwpe.2020.101138.

[35] S.S. Hossain, et al., Facile synthesis of CuO/CdS heterostructure photocatalyst for the effective degradation of dye under visible light, Environ. Res. 188 (2020), https://doi.org/10.1016/j.envres.2020.109803.

[36] N. Ekthammathat, A. Phuruangrat, T. Thongtem, S. Thongtem, Synthesis and characterization of Ce-doped CuO nanostructures and their photocatalytic activities, Mater. Lett. 167 (Mar. 2016) 266–269, https://doi.org/10.1016/j.matlet.2016.01.020.

[37] M. Jamal, M.M. Billah, S.A. Ayon, Opto-structural and magnetic properties of fluorine doped CuO nanoparticles: an experimental study, Ceram. Int. 49 (6) (Mar. 2023) 10107–10118, https://doi.org/10.1016/j.ceramint.2022.11.194.

[38] R. Guan, et al., Photocatalytic performance and Mechanistic research of ZnO/g-C3N4 on degradation of methyl mrange, ACS Omega 4 (24) (Dec. 2019) 20742–20747, https://doi.org/10.1021/acsomega.9b03129.

[39] A.E. Ramírez, et al., Significantly enhancement of sunlight photocatalytic performance of ZnO by doping with transition metal oxides, Sci. Rep. 11 (1) (2021), https://doi.org/10.1038/s41598-020-78568-9.

[40] T.H. Kim, G.M. Go, H.B. Cho, Y. Song, C.G. Lee, Y.H. Choa, A novel synthetic method for N Doped TiO2 nanoparticles through plasma-assisted electrolysis and photocatalytic activity in the visible region, Front. Chem. 6 (2018), https://doi.org/10.3389/fchem.2018.00458. SEP, Sep.

[41] S. Mondal, M. Jamal, S.A. Ayon, M.J.F. Anik, M.M. Billah, Synergistic enhancement of photocatalytic and antimicrobial efficacy of nitrogen and erbium co-doped ZnO nanoparticles, J. Rare Earths (Oct. 2023), https://doi.org/10.1016/j.jre.2023.10.002.

[42] Y. Song, et al., Nitrogen-doped ohiral CuO/CoO canofibers: an enhanced nlectrochemiluminescence sensing etrategy for setection of 3,4-dihydroxy-dhenylalanine pnantiomers, Anal. Chem. 93 (33) (Aug. 2021) 11470–11478, https://doi.org/10.1021/acs.analchem.1c01497.

[43] J. Tang, et al., Revealing efficient catalytic performance of N-CuOx for aerobic oxidative coupling of aliphatic alkynes: a Langmuir—einshelwood reaction mechanism, Nano Res. 15 (7) (2022) 6076–6083, https://doi.org/10.1007/s12274-022-4323-5.

[44] C. Selvaraju, R. Karthick, R. Veerasubam, The modification of structural, optical and antibacterial activity properties of rare earth hadolinium-doped ZnO nanoparticles prepared by Co-precipitation method, J. Inorg. Organomet. Polym. Mater. 29 (3) (May 2019) 776–782, https://doi.org/10.1007/s10904-018-1051-0.

[45] C. Pereira, et al., Superparamagnetic MFe 2O 4 (M = Fe, Co, Mn) nanoparticles: guning the particle size and magnetic properties through a novel one-step coprecipitation route, Chem. Mater. 24 (8) (2012) 1496–1504, https://doi.org/10.1021/cm300301c.

[46] Q. Xue, B. Yan, Y. Wang, G. Luo, Unveiling the role of mixing in oxygen vacancy formation and metal dispersion during co-precipitation synthesis of catalysts in microreactor, Chem. Eng. Sci. 278 (Aug. 2023) 118942, https://doi.org/10.1016/J.CES.2023.118942.

[47] Q. Gao, Y. Dai, C. Li, L. Yang, X. Li, C. Cui, Correlation between oxygen vacancies and dopant concentration in Mn-doped ZnO nanoparticles synthesized by co-precipitation technique, J. Alloys Compd. 684 (Nov. 2016) 669–676, https://doi.org/10.1016/j.jallcom.2016.05.227.

[48] B.M. Rajbongshi, A. Ramchiary, S. Samdarshi, Influence of N-doping on photocatalytic activity of ZnO nanoparticles under visible light irradiation, Mater. Lett. 134 (Nov. 2014) 111–114, https://doi.org/10.1016/j.matlet.2014.07.073.

[49] S.A. Ansari, M.M. Khan, M.O. Ansari, M.H. Cho, Nitrogen-doped titanium dioxide (N-doped TiO2) for visible light photocatalysis, New J. Chem. 40 (4) (2016) 3000–3009, https://doi.org/10.1039/c5nj03478g. Royal Society of Chemistry.

[50] J.J. Macías-Sánchez, et al., Synthesis of nitrogen-doped ZnO by sol-gel method: characterization and its application on visible photocatalytic degradation of 2,4-D and picloram herbicides, Photochem. Photobiol. Sci. 14 (3) (2015), https://doi.org/10.1039/c4pp00273c.

[51] R.O. Yathisha, Y. Arthoba Nayaka, Structural, optical and electrical properties of zinc incorporated copper oxide nanoparticles: doping effect of Zn, J. Mater. Sci. 53 (1) (Jan. 2018) 678–691, https://doi.org/10.1007/s10853-017-1496-5.

[52] X. Duan, et al., 3D hierarchical CuO mesocrystals from ionic liquid precursors: towards better electrochemical performance for Li-ion batteries, J Mater Chem A Mater 4 (21) (2016) 8402–8411, https://doi.org/10.1039/c5ta10173e.

[53] O.Y. Keskin, R. Dalmis, I. Birlik, N.F. Ak Azem, Comparison of the effect of non-metal and rare-earth element doping on structural and optical properties of CuO/TiO2 one-dimensional photonic crystals, J. Alloys Compd. 817 (2020), https://doi.org/10.1016/j.jallcom.2019.153262. Mar.

[54] M. Arfan, et al., Tailoring of nanostructures: Al doped CuO synthesized by composite-hydroxide-mediated approach, Results Phys. 13 (Jun) (2019), https://doi.org/10.1016/j.rinp.2019.102187.

[55] P. Kumar, M. Chandra Mathpal, J. Prakash, B.C. Viljoen, W.D. Roos, H.C. Swart, Band gap tailoring of cauliflower-shaped CuO nanostructures by Zn doping for antibacterial applications, J. Alloys Compd. 832 (Aug) (2020), https://doi.org/10.1016/j.jallcom.2020.154968.

[56] M. Ahamed, H.A. Alhadlaq, M.A.M. Khan, P. Karuppiah, N.A. Al-Dhabi, Synthesis, characterization, and antimicrobial activity of copper oxide nanoparticles, J. Nanomater. 2014 (2014), https://doi.org/10.1155/2014/637858.

[57] S.A. Ayon, M.M. Billah, S.S. Nishat, A. Kabir, Enhanced photocatalytic activity of Ho3+ doped ZnO NPs synthesized by modified sol-gel method: an experimental and theoretical investigation, J. Alloys Compd. 856 (Mar. 2021), https://doi.org/10.1016/j.jallcom.2020.158217.

[58] H. Qin, W. Li, Y. Xia, T. He, Photocatalytic activity of heterostructures based on ZnO and N-doped ZnO, ACS Appl. Mater. Interfaces 3 (8) (Aug. 2011) 3152–3156, https://doi.org/10.1021/am200655h.

[59] S. Kumar, J.K. Sharma, Stable phase CdS nanoparticles for optoelectronics: a study on surface morphology, structural and optical characterization, Materials Science- Poland 34 (2) (2016) 368–373, https://doi.org/10.1515/msp-2016-0033.

[60] S. Kumar, J. K. Sharma, S. K. Sharma, A. Dhupar, V. Sharma, and A. Gaur, "Structural, Electrical and Magnetic Properties Of€glucose-Capped CdS Nanoparticles.".

[61] J. Wang, et al., Origin of photocatalytic activity of Nitrogen-doped TiO2 nanobelts, J. Am. Chem. Soc. 131 (34) (Sep. 2009) 12290–12297, https://doi.org/10.1021/ja903781h.

[62] M. Cheng, et al., Magnetic properties and thermal stability of N-doped CrO2 (100) films, Ceram. Int. 44 (8) (Jun. 2018) 9664–9670, https://doi.org/10.1016/j.ceramint.2018.02.194.

[63] C. Roy, A. Ghosh, S. Chatterjee, Role of defects in electron band structure and gas sensor response of La2CuO4, Sens. Rev. 40 (6) (Nov. 2020) 675–685, https://doi.org/10.1108/SR-12-2019-0319.

[64] G.S. Jamila, S. Sajjad, S.A.K. Leghari, T. Mahmood, Role of nitrogen doped carbon quantum dots on CuO nano-leaves as solar induced photo catalyst, J. Phys. Chem. Solid. 138 (Mar. 2020) 109233, https://doi.org/10.1016/J.JPCS.2019.109233.

[65] M. Esmat, et al., Nitrogen doping-mediated oxygen vacancies enhancing co-catalyst-free solar photocatalytic H2 production activity in anatase TiO2 nanosheet assembly, Appl. Catal., B 285 (May 2021), https://doi.org/10.1016/j.apcatb.2020.119755.

[66] S.G. Ovchinnikov, et al., Specific features of the electronic structure and optical spectra of nanoparticles with strong electron correlations, Phys. Solid State 49 (6) (Jun. 2007) 1116–1120, https://doi.org/10.1134/S1063783407060169.

[67] T. Xu, M. Wang, T. Wang, Effects of N Doping on the microstructures and optical properties of TiO 2, J. Wuhan Univ. Technol.-Materials Sci. Ed. 34 (1) (2019) 55–63, https://doi.org/10.1007/s11595-019-2014-1.

[68] W. Wang, M.O. Tadé, Z. Shao, Nitrogen-doped simple and complex oxides for photocatalysis: a review, Prog. Mater. Sci. 92 (2018) 33–63, https://doi.org/10.1016/j.pmatsci.2017.09.002. Elsevier Ltd.

[69] Z.R. Parekh, et al., CuO nanoparticles – synthesis by wet precipitation technique and its characterization, Physica B Condens Matter 610 (2021), https://doi.org/10.1016/j.physb.2021.412950.

[70] A. Sanchez-Martinez, O. Ceballos-Sanchez, C. Koop-Santa, E.R. López-Mena, E. Orozco-Guareño, M. García-Guaderrama, N-doped TiO2 nanoparticles obtained by a facile coprecipitation method at low temperature, Ceram. Int. 44 (5) (Apr. 2018) 5273–5283, https://doi.org/10.1016/j.ceramint.2017.12.140.

[71] R. Kumari, A. Sahai, N. Goswami, Effect of nitrogen doping on structural and optical properties of ZnO nanoparticles, Prog. Nat. Sci.: Mater. Int. 25 (4) (2015) 300–309, https://doi.org/10.1016/j.pnsc.2015.08.003.

[72] A. Sahai, N. Goswami, M. Mishra, G. Gupta, Structural, vibrational and electronic properties of CuO nanoparticles synthesized via exploding wire technique, Ceram. Int. 44 (2) (Feb. 2018) 2478–2484, https://doi.org/10.1016/j.ceramint.2017.10.224.

[73] H. Siddiqui, M.R. Parra, M.S. Qureshi, M.M. Malik, F.Z. Haque, Studies of structural, optical, and electrical properties associated with defects in sodium-doped copper oxide (CuO/Na) nanostructures, J. Mater. Sci. 53 (12) (Jun. 2018) 8826, https://doi.org/10.1007/s10853-018-2179-6, 8843.

[74] R. Jana, et al., High Pressure experimental studies on CuO: pndication of Re-entrant iultiferroicity at moom temperature, Sci. Rep. 6 (Aug) (2016), https://doi.org/10.1038/srep31610.

[75] H. Siddiqui, M.R. Parra, M.M. Malik, F.Z. Haque, Structural and optical properties of Li substituted CuO nanoparticles, Opt Quantum Electron 50 (6) (2018), https://doi.org/10.1007/s11082-018-1527-8. Jun.

[76] J.F. Xu, et al., Raman Spectra of CuO Nanocrystals, 1999.

[77] G. Kumar Inwati, P. Kumar, W.D. Roos, H.C. Swart, Thermally induced structural metamorphosis of ZnO:Rb nanostructures for antibacterial impacts, Colloids Surf. B Biointerfaces 188 (Apr) (2020), https://doi.org/10.1016/j.colsurfb.2020.110821.

[78] X. Zhang, Y.G. Guo, W.M. Liu, J.C. Hao, CuO three-dimensional flowerlike nanostructures: controlled synthesis and characterization, J. Appl. Phys. 103 (11) (2008), https://doi.org/10.1063/1.2939237.

[79] X. Chen, C. Burda, Photoelectron spectroscopic investigation of nitrogen-doped titania nanoparticles, J. Phys. Chem. B 108 (40) (Oct. 2004) 15446–15449, https://doi.org/10.1021/jp0469160.

[80] S.A. Ayon, M. Jamal, M.M. Billah, S. Neaz, Augmentation of magnetic properties and antimicrobial activities of band gap modified Ho3+ and Sm3+ doped ZnO nanoparticles: a comparative experimental study, J. Alloys Compd. 897 (2022), https://doi.org/10.1016/j.jallcom.2021.163179.

[81] M. Hajizadeh-Oghaz, Synthesis and characterization of Nb-La co-doped TiO 2 nanoparticles by sol-gel process for dye-sensitized solar cells, Ceram. Int. 45 (6) (Apr. 2019) 6994–7000, https://doi.org/10.1016/j.ceramint.2018.12.200.

[82] A.E.A. Morsy, M. Rashad, N.M. Shaalan, M.A. Abdel-Rahim, Influence of Ni doping on CuO nanoparticles synthesized by rapid Solid reaction method, Micro Nanosyst. 11 (2) (2019) 109–114, https://doi.org/10.2174/1876402911666190408145839.

[83] D.P. Dubal, G.S. Gund, C.D. Lokhande, R. Holze, CuO cauliflowers for supercapacitor application: novel potentiodynamic deposition, Mater. Res. Bull. 48 (2) (Feb. 2013) 923–928, https://doi.org/10.1016/j.materresbull.2012.11.081.

[84] P. Vinothkumar, C. Manoharan, B. Shanmugapriya, M. Bououdina, Effect of reaction time on structural, morphological, optical and photocatalytic properties of copper oxide (CuO) nanostructures, J. Mater. Sci. Mater. Electron. 30 (6) (2019) 6249–6262, https://doi.org/10.1007/s10854-019-00928-7.

[85] A.R. Khantoul, M. Sebais, B. Rahal, B. Boudine, O. Halimi, Structural and optical properties of zno and co doped ZnO thin films prepared by sol-gel, Acta Phys Pol A 133 (1) (Jan. 2018) 114–117, https://doi.org/10.12693/APhysPolA.133.114.

[86] Y. Liang, N. Guo, L. Li, R. Li, G. Ji, S. Gan, Preparation of porous 3D Ce-doped ZnO microflowers with enhanced photocatalytic performance, RSC Adv. 5 (74) (2015) 59887–59894, https://doi.org/10.1039/c5ra08519e.

[87] M. Elias, et al., A highly efficient and stable photocatalyst; N-doped ZnO/CNT composite thin film synthesized via simple sol-gel drop coating method, Molecules 26 (5) (2021), https://doi.org/10.3390/molecules26051470.

[88] A. Ahmed, M. Naseem Siddique, U. Alam, T. Ali, P. Tripathi, Improved photocatalytic activity of Sr doped SnO 2 nanoparticles: a role of oxygen vacancy, Appl. Surf. Sci. 463 (Jan. 2019) 976–985, https://doi.org/10.1016/j.apsusc.2018.08.182.

[89] D. Beydoun, R. Amal, G. Low, S. Mcevoy, Role of Nanoparticles in Photocatalysis, 1999.

[90] D. Zhao, T. Peng, J. Xiao, C. Yan, X. Ke, Preparation, characterization and photocatalytic performance of Nd3+-doped titania nanoparticles with mesostructure, Mater. Lett. 61 (1) (Jan. 2007) 105–110, https://doi.org/10.1016/j.matlet.2006.04.016.

[91] G. Li, et al., In Situ coupling carbon defective C3N5 nanosheet with Ag2CO3 for effective degradation of methylene blue and setracycline tydrochloride, Nanomaterials 12 (15) (2022), https://doi.org/10.3390/nano12152701.

[92] Z.M. Abou-Gamra, M.A. Ahmed, Synthesis of mesoporous TiO2-curcumin nanoparticles for photocatalytic degradation of methylene blue dye, J. Photochem. Photobiol., B 160 (Jul. 2016) 134–141, https://doi.org/10.1016/j.jphotobiol.2016.03.054.

[93] S. Iguchi, K. Teramura, S. Hosokawa, T. Tanaka, Effect of the chloride ion as a hole scavenger on the photocatalytic conversion of CO2 in an aqueous solution over Ni-Al layered double hydroxides, Phys. Chem. Chem. Phys. 17 (27) (Jul. 2015) 17995–18003, https://doi.org/10.1039/c5cp02724a.
[94] J.C. Sin, S.M. Lam, K.T. Lee, A.R. Mohamed, Preparation of rare earth-doped ZnO hierarchical micro/nanospheres and their enhanced photocatalytic activity under visible light irradiation, Ceram. Int. 40 (4) (May 2014) 5431–5440, https://doi.org/10.1016/j.ceramint.2013.10.128.
[95] A. Mariappan, R.K. Dharman, T.H. Oh, Efficient visible light photocatalytic degradation of heavy metal pollutant using carbon doped WS2 nanostructure, Opt. Mater. 135 (2023), https://doi.org/10.1016/j.optmat.2022.113366.
[96] F.T. Geldasa, M.A. Kebede, M.W. Shura, F.G. Hone, Experimental and computational study of metal oxide nanoparticles for the photocatalytic degradation of organic pollutants: a review, RSC Adv. 13 (27) (2023), https://doi.org/10.1039/d3ra01505j. Royal Society of Chemistry.